Elastic scattering phenomenological analysis of the first resonant structure of the $^{28}Si + {}^{16}O$ system

M. C. Mermaz, E. R. Chavez-Lomeli, J. Barrette, B. Berthier, and A. Greiner
Département de Physique Nucléaire/Basse Energie, Saclay, 91191 Gif-sur-Yvette Cedex, France
(Received 27 June 1983)

Seven elastic scattering angular distributions have been measured for the system $^{16}O + {}^{28}Si$ around the first resonant structure observed in the $\theta_{c.m.} = 180°$ excitation function at 21.1 MeV center of mass energy just above the Coulomb barrier. Optical model, Regge pole, and phase shift analyses have been performed. These complementary analyses show that several partial waves contribute to the backward rise and the oscillatory behavior of the elastic scattering angular distributions. The 21.1 MeV resonant structure can be interpreted in terms of several overlapping resonances. Tentative spin assignments are made for these states.

[NUCLEAR REACTIONS Elastic scattering of $^{28}Si(^{16}O,{}^{16}O)$. Seven angular distributions measured between 18.67 and 22.29 MeV, angular range 25° to 176° c.m. Optical model, Regge pole, and phase shift analyses.]

I. INTRODUCTION

Elastic scattering of the $^{28}Si + {}^{16}O$ system has been already extensively studied over a wide range of energy from the Coulomb barrier at 17 MeV up to a center of mass energy of 65 MeV.[1] An excitation function at 180° c.m. angle and several angular distributions have been measured. The excitation function is characterized by regular 1-MeV wide resonance structures on which are superimposed a finer structure of roughly 200 keV width.

The angular distributions are qualitatively reproduced by optical model and/or Regge pole analyses except at very low incident energy. A weakness of optical model analysis is that the parameters, which define the already very sophisticated potential shape, fluctuate rapidly with the incident energy. These fluctuations are in disagreement with the concept of mean field.[2] Therefore, it can be considered that the erratic behavior of such a potential hides other phenomena such as resonances of a composite system. It has turned out that it is impossible to correlate a given spin, tentatively extracted from one angular distribution, with a given bump seen in the excitation function.[1] This means that a bump is not a well-defined resonance of the composite system.

Analysis based on statistical fluctuation of the scattering matrix with respect to a background given by a diffractional model has been successful and shows that possibly many overlapping resonances contribute to the sophisticated shapes of the angular distributions, in particular, at high incident energy: 31.82 and 35.00 MeV center of mass energy.[3] In this picture, it is at present not clear how these many overlapping resonances would add up coherently to results in the relatively regular broad structure observed in the large angle excitation function.

In light of such puzzling results, we have decided to study in more detail the first structure of the 180° c.m. excitation function located at 21 MeV center of mass energy, just above the Coulomb barrier where simple phenomena can be expected owing to low excitation energy in the composite system and also owing to the few partial wave numbers involved in the elastic scattering. In addition to a previous angular distribution already measured by the Brookhaven National Laboratory (BNL) group,[1] we have measured seven other angular distributions between 18.67 and 22.29 MeV center of mass energy in order to study the resonant mechanism and the hypothetical possibility of spin assignments for such a structure.

After the description of the experimental procedure, we shall present an optical model, Regge pole, and phase shift analyses of the data. These three different analyses, more or less complementary, allow us to understand that resonance phenomena are present but that more than one resonance is necessary to explain the shape of the eight elastic scattering angular distributions measured in this narrow energy region.

II. EXPERIMENTAL PROCEDURE

Seven angular distributions have been measured from a pure Rutherford region ($\theta_{c.m.} \simeq 25°$) up to 176° center of mass angle, using the inverse reaction (^{28}Si beam on a ^{16}O target) for the backward center of mass angles ($\theta_{c.m.} \geq 100°$). In the backward angle range, we have used the ^{28}Si beam of the super FN tandem Van de Graaff of Saclay and a 100 $\mu g/cm^2$ self-supporting SiO target. The ^{16}O recoil nuclei were detected at forward angles by a QDDD magnetic spectrometer. In front of the gas

counter, which was located at the focal plane, Havar foils were installed in order to stop the ^{28}Si scattered particles. This setup has been already described in a previous paper.[4] The forward angle angular distributions were measured using the ^{16}O beam and a 30 μg/cm^2 enriched ^{28}Si target on carbon backing. Particles were detected using at very forward angles a collimated position sensitive solid state counter giving seven angles simultaneously and, for the intermediate angles, a ΔE-E solid state telescope in order to achieve a better energy separation between the first 2^+ and g.s. of the ^{28}Si target nucleus. In both experiments, two solid state monitors, placed left and right with respect to the beam axis, were used in order to correct beam alignment instability. Between the backward and forward data, there was a 10° overlapping region for normalization. The absolute values were obtained by the normalization on the pure Rutherford value at forward angles. The energy given in the paper corresponds to the target center using the Northcliffe and Schilling tables to correct for energy loss.[5] Charge state corrections for the yields obtained from the QDDD spectrometer are done using the tables of Marion and Young.[6]

In Fig. 1, the $\theta_{c.m.} = 180°$ excitation function for the ^{16}O+^{28}Si is presented and the seven energies at which new elastic angular distributions have been measured are indicated by arrows. These angular distributions together with the angular distribution measured previously at 21.1 MeV (Ref. 1) are shown in Fig. 2. All of the angular distributions present oscillatory behavior at backward angles. It is also observed that the angular distribution corresponding to the minimum of the excitation function at $E_{c.m.} = 19.5$ MeV has a deep minimum near $\theta_{c.m.} = 180°$. This observation has been the subject of an earlier report.[7]

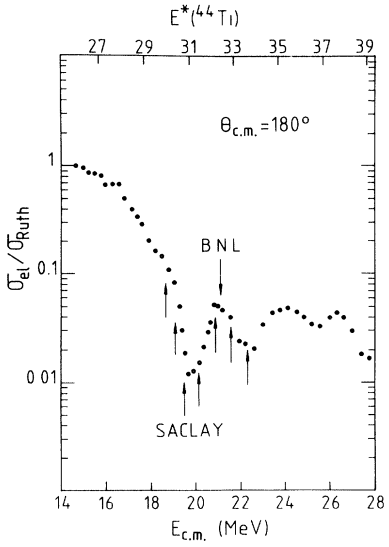

FIG. 1. Excitation function at 180° center of mass for the ^{28}Si+^{16}O elastic scattering measured just above the Coulomb barrier. The arrows indicate the energies where angular distributions have been measured. The data points are from a group at Brookhaven National Laboratory (Ref. 1).

III. DISCUSSION

A. Optical model analysis

The dashed curves in Fig. 2 are six parameter fits obtained assuming a volume Wood-Saxon optical potential for both the real and imaginary parts. The resulting potential parameters are listed in Table I. This analysis is done with the automatic-search code ECIS of Raynal. The starting value for the real potential depth was very large in conformity with potentials obtained from a double folding procedure.[2] The general qualitative agreement with the data is good; however, at low energy the calculated angular distributions fail to reproduce the weak oscillatory

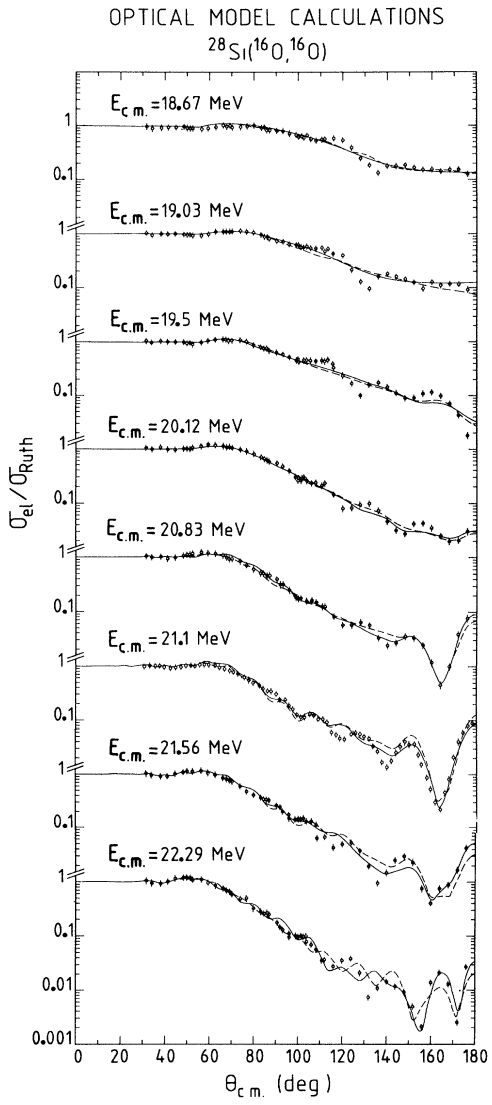

FIG. 2. Experimental elastic scattering angular distribution of the ^{16}O+^{28}Si system. The solid curves are optical model fits using a deep transparent potential with surface correction terms; the dashed curves are for the same types of potentials but without correction terms. These results are from the ECIS FORTRAN code of Raynal (see the text).

TABLE I. Optical model parameters.

E (MeV)	χ^{2a}	V (MeV)	R_V (fm)	a_V (fm)	W (MeV)	R_W (fm)	a_W (fm)
18.67	1.94	554.8	7.076	0.331	392.8	0.796	0.025
19.03	4.22	676.6	6.290	0.422	511.6	0.845	0.025
19.5	4.12	677.0	6.290	0.423	520.0	0.839	0.025
20.12	2.17	769.8	5.836	0.480	494.3	0.831	0.025
20.83	2.60	689.5	6.236	0.438	453.5	0.871	0.025
21.1	7.58	683.1	6.270	0.452	974.5	0.882	0.025
21.56	6.89	768.9	5.872	0.468	726.0	0.849	0.025
22.29	9.28	744.3	6.032	0.448	246.2	0.915	0.025
18.67	2.49	100.9	6.649	0.515	49.36	3.387	0.025
19.03	3.41	139.5	5.621	0.670	176.50	3.050	0.025
19.5	5.81	88.34	6.484	0.552	89.03	2.875	0.025
20.12	3.93	86.94	6.530	0.583	89.59	2.890	0.025
20.83	4.23	86.94	6.526	0.583	89.59	2.890	0.025
21.1	6.55	77.20	6.822	0.539	46.80	2.925	0.025
21.56	9.02	77.60	6.833	0.503	51.02	2.865	0.025
22.29	18.83	77.59	6.842	0.504	35.02	2.977	0.025

$^a\chi^2=\frac{1}{N}\sum_{i=1}^{N}\left[\frac{\sigma^i_{\text{exp}}-\sigma^i_{\text{theo}}}{\Delta\sigma^i_{\text{exp}}}\right]^2$; 10% error bars.

structure at large angles. The calculated distributions just go through the average of all the data points. To reproduce the oscillatory behavior at the highest energies, it was necessary to use a very large transparency. The radius of the imaginary part is only about 1 fm as compared to 6 fm for the radius of the real part of the potential. Let us also note that the diffuseness parameter for the imaginary part is extremely small compared to the incoming local wavelength. This transparency and small value of the diffusivity is directly responsible for the backward rise and oscillatory behavior of the angular distributions. A very large transparency of the potential near the barrier was also deduced from a recent optical model analysis based on a slightly corrected double-folded potential.[2] Other solutions with a depth nearer to 100 MeV for the real part of the potential have been tried and provided poorer fits as can be seen by the tabulated values of χ^2 in Table I. However, the resulting transparency of the shallower potential is comparable to that obtained with the deeper potential.

Contrary to what might be expected, the very large transparency results nevertheless in reasonable reaction cross sections. The calculated cross sections are plotted in Fig. 3. These reaction cross sections are roughly 20% higher than the experimental fusion cross sections measured for $^{16}O+^{28}Si$ in the same energy range.[8] This is consistent with the expected contributions from inelastic scattering and direct transfer to the reaction cross sections.

In order to improve the overall quality of the fits, two corrections of surface derivative Wood-Saxon form were added for the 700 MeV real depth family of potentials. The value of the fitted parameters are presented in Table II and the corresponding angular distributions are shown in Fig. 2 by a solid line. The quality of the fits is indeed improved. We do not understand at present the meaning of such terms which vary so rapidly with energy. It has been speculated that the surface correction terms are owing to some coupling effects between the elastic channel and the inelastic excitation of the first 2^+ state in ^{28}Si[2]. Alternatively, the fast variations of the optical model parameters might also mask resonance phenomena belonging to the formation of a composite dinuclear system.

The real and imaginary effective optical model potential with surface correction terms at 21.1 MeV is plotted in

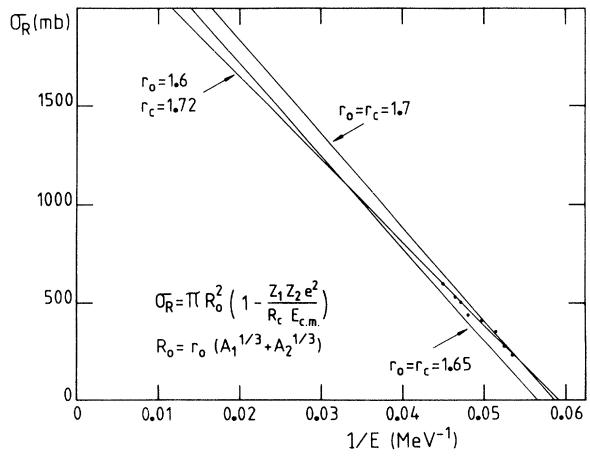

FIG. 3. Total reaction cross section: The points are given by the optical model calculations and are compared to the sharp cutoff predictions of the diffractional model.

TABLE II. Optical model parameters.

		Volume real part[a]			Surface real part[a]						Volume imaginary part[b]		
$E_{c.m.}$ (MeV)	χ^2	V_0 (MeV)	R_V (fm)	a_V (fm)	V_1 (MeV)	R_1 (fm)	a_1 (fm)	V_2 (MeV)	R_2 (fm)	a_2 (fm)	W (MeV)	R_W (fm)	a_W (fm)
22.29	7.27	675	6.34	0.422	−244	6.19	0.089	0.196	8.95	0.362	931	0.948	0.036
21.56	3.63	696	6.24	0.422	−241	5.89	0.087	0.400	7.66	0.458	1045	0.853	0.036
21.1	3.94	693	6.23	0.437	−242	5.90	0.091	0.736	7.64	0.454	785	0.826	0.036
20.83	3.45	693	6.21	0.437	−203	5.88	0.059	−8.210	6.08	0.535	899	0.795	0.036
20.12	2.02	674	6.33	0.437	−270	5.99	0.080	0.446	6.48	0.194	909	0.852	0.036
19.50	4.35	682	6.33	0.442	−302	5.99	0.113	1.455	4.957	0.222	1709	0.838	0.036
19.03	2.56	632	6.61	0.422	−313	6.41	0.091	1.549	9.03	0.035	1886	1.035	0.036
18.67	1.83	632	6.61	0.422	−311	6.41	0.092	0.309	8.98	0.257	1845	1.030	0.036

[a] $$V(r) = -V_0 \frac{1}{1+\exp\frac{r-R_v}{a_v}} - \sum_{i=1}^{2} 4a_i V_i \frac{d}{dr} \frac{1}{1+\exp\frac{r-R_i}{a_i}}.$$

[b] $$W(r) = -W \frac{1}{1+\exp\frac{r-R_W}{a_W}}.$$

Fig. 4 for the partial waves $l=0$ to 20 with a step of 5. As stated above, features common to all of the potentials are very large transparencies and a small value of the diffuseness parameter for the imaginary part. The location of the imaginary potential with respect to the inner part of the centrifugal barrier explains that in spite of its very large transparency, this potential is still strongly absorbing for the partial waves smaller than the grazing wave which at this energy is approximately $l_g = 10$. The necessity to maintain a strong absorption for $l < l_g$ explains why for the shallower potentials the radius of the imaginary potential becomes significantly larger than for the deeper potentials (see Table I).

To evaluate the importance of inelastic excitation, a coupled channel analysis has been performed in which the ground state and 1.78 MeV 2^+ states were coupled in a harmonic vibrational mode. The potentials resulting from an automatic search are given in Table III and a typical example of a fit is provided in Fig. 5. It turns out that the fits are worse than in the case of pure elastic scattering analysis, but the important conclusion is that the coupled channel calculation does not change at all the qualitative aspect of the optical potentials: compare Tables II and III. This means that in the present analysis, the coupling does not play a predominant role in explaining the resonance behavior experimentally observed in the excitation function.

Argand-Cauchy plots of the scattering matrices for the 700 MeV deep potentials of Table II, corresponding to the best fits solid lines of Fig. 2, are presented in Fig. 6. The behavior of the S-matrix elements is highly irregular. However, the Argand-Cauchy plots seem to often contain the kind of loops which could be a signature of relatively narrow (i.e., near the real axis) Regge poles in the S matrix. As already shown in the literature, the large transparency associated with deep real potential gives rise to such poles.[9] To study the importance of isolated narrow poles in explaining the structured angular distributions at larger angles, the next subsection will present an analysis where such poles are taken explicitly into account.

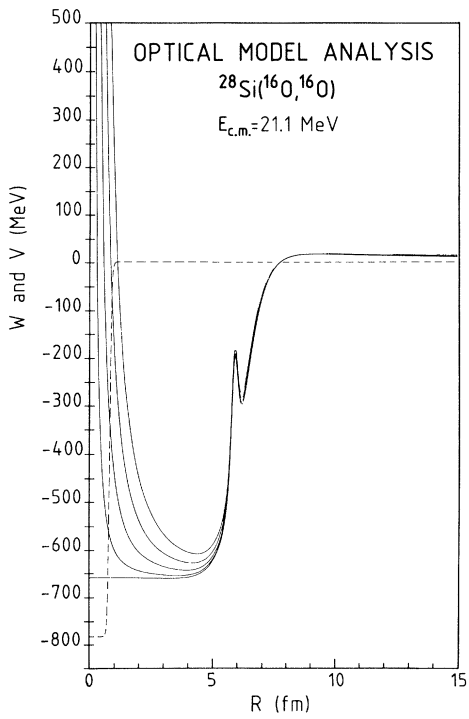

FIG. 4. Plot of the real and imaginary part of the effective optical model potential with surface correction terms for the partial waves $l=0$, 5, 10, 15, and 20. Let us note the large transparency of such a potential.

TABLE III. Coupled channel parameters.

	Optical model parameters											
E (MeV) c.m.	V (MeV)	R_V (fm)	a_V (fm)	V_1 (MeV)	R_1 (fm)	a_1 (fm)	V_2 (MeV)	R_2 (fm)	a_2 (fm)	W (MeV)	R_W (fm)	a_W (fm)
21.56	696	6.23	0.422	−242	5.89	0.089	0.40	7.66	0.458	622	0.882	0.021
21.1	693	6.23	0.437	−201	5.89	0.116	6.27	6.73	0.454	723	0.886	0.021
20.83	693	6.23	0.437	−194	5.89	0.112	2.03	7.21	0.374	723	0.886	0.021
20.12	674	6.33	0.437	−219	6.01	0.121	9.79	6.95	0.224	885	0.846	0.039
19.5	680	6.33	0.438	−280	5.99	0.114	−12.6	5.47	0.717	1616	0.824	0.064

		Potential coupling parameters						
E (MeV) c.m.	χ^2	V (MeV)	R_V (fm)	a_V (fm)	W (MeV)	R_W (fm)	a_W (fm)	β_2
21.56	4.84	605	6.24	0.501	96.0	6.12	0.038	0.643
21.1	10.44	700	6.11	0.466	88.7	6.11	0.032	0.348
20.83	4.76	662	6.10	0.485	73.5	6.11	0.028	0.417
20.12	2.97	584	6.63	0.542	108.0	6.31	0.051	0.615
19.5	5.84	634	6.26	0.539	113.0	6.32	0.038	0.554

B. Regge pole analysis

This analysis has been performed using the nuclear scattering amplitude, with the usual notations, in the following expression:

$$f_N(\theta)=\frac{i}{2k}\sum_{l=0}^{\infty}(2l+1)e^{2i\sigma_l}(1-S_l)P_l(\cos\theta)\ . \tag{1}$$

The scattering matrix elements S_l are parametrized as follows:

$$S_l=S(\mathrm{BG})+\frac{iD(l)e^{i\phi_{l_0}}}{l-l_0-\frac{i\Gamma(l)}{2}} \tag{2}$$

with the following Frahn and Venter parametrization for the background (BG) (Ref. 10)

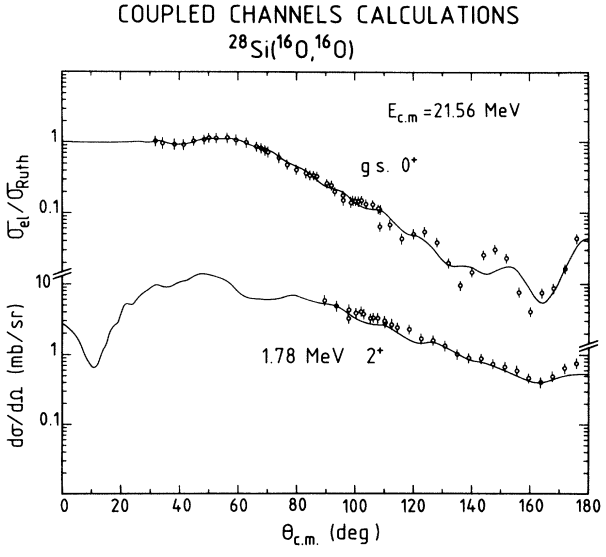

FIG. 5. Coupled channel calculations of the elastic scattering and first 2^+ inelastic scattering of ^{28}Si, using the harmonic vibrational model with a $\beta_2=0.643$.

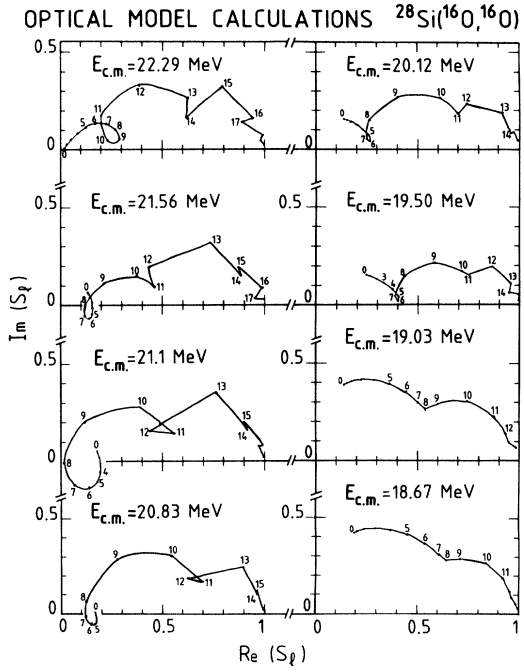

FIG. 6. Argand-Cauchy plot of the total S-matrix elements of the optical model fits (solid curve) of Fig. 2.

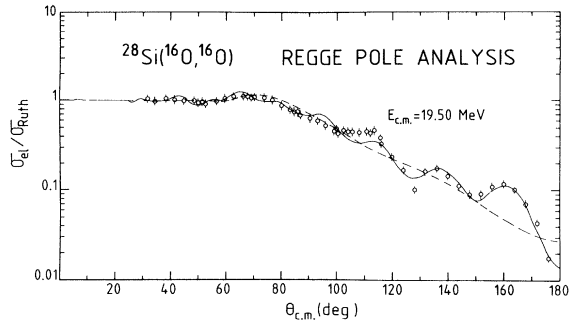

FIG. 7. Regge pole calculated angular distributions (solid line). The dashed curve corresponds to the S_l(BG) background matrix elements alone of the diffractional model. The corresponding parameters are listed in Table III.

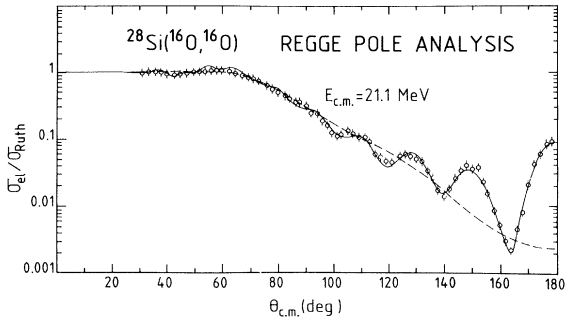

FIG. 8. See the caption of Fig. 7.

$$S_l(\mathrm{BG})=[1+\exp(l_g-l)/\Delta]^{-1} + i\mu\frac{\partial}{\partial l}[1+\exp(l_g-l)/\Delta]^{-1} .$$

The amplitude $D(l)$ and the width $\Gamma(l)$ of the pole are expressed as follows:

$$D(l)=D_0[1-R_e S_l(\mathrm{BG})] , \quad (3)$$

$$\Gamma(l)=\Gamma_0[1-R_e S_l(\mathrm{BG})] . \quad (4)$$

The quantities between brackets are just the usual damping function used in order to avoid spurious angular-distribution oscillations owing to high orbital angular momentum cutoff in the computation. The quantities ϕ_{l_0} and l_0 are, respectively, the phase and orbital angular momentum of the pole. The grazing angular momentum l_g and the width Δ are related to the radius and the diffusivity parameter through the two following semiclassical formulas, where R and η are, respectively, the radius and Sommerfeld parameter:

$$l_g=kR\left[1-\frac{2\eta}{kR}\right]^{1/2} , \quad (5)$$

$$\Delta=kd\left[1-\frac{\eta}{kR}\right]\left[1-\frac{2\eta}{kR}\right]^{-1/2} , \quad (6)$$

with

$$R=r_0(A_p^{1/3}+A_T^{1/3}) .$$

In Figs. 7 and 8, the results of the Regge pole analysis for the angular distributions, measured on the first minimum and first maximum of the 180° c.m. excitation function, respectively, are presented (see Fig. 1). The dashed curve is owing to the background term alone of the scattering matrix while the solid line represents the full calculation including the Regge pole. The seven parameters r_0, d, μ, ϕ_0, D_0, Γ_0, and l_0 have been searched simultaneously in order to produce the best fits to the data. The values of the parameters are listed in Table IV.

In Figs. 9 and 10, the results of the Regge pole fits for the intermediate energies around the first structure of the excitation function, which are identical to the calculations in Figs. 7 and 8, are presented. The corresponding parameters are given in Table IV. The quality of the fits is excellent with, perhaps, the exception of the lowest energies where the phase of the last oscillation is not perfectly reproduced. In fact, at the two lowest energies, 18.67 and 19.03 MeV, the width Γ_0 is extremely small and the calculation is equivalent to a single $l=3$ resonance. The excitation function has no clear resonant structure in this energy region, but just a small shoulder owing to the very fast variation with energy of the background (see Fig. 1). For all the other energies, the widths are much larger and show that several partial waves, three to four, contribute to the oscillatory pattern of the angular distribution. The

TABLE IV. Regge pole analysis parameters. L_g: see formula (5); Δ: see formula (6).

$E_{c.m.}$ (MeV)	L_g	L_0	ϕ_{l_0}	Γ	D	r_0	d	$\mu/4\Delta$	χ^2
18.67	5.55	3.0	220.1	0.03	0.01	1.634	0.430	0.11	0.85
19.03	6.96	3.0	289.0	0.07	0.03	1.643	0.448	0.39	1.38
19.50	7.87	8.05	76.6	2.50	1.09	1.634	1.09	0.56	1.34
20.12	8.42	7.05	56.91	1.123	0.32	1.605	0.32	0.40	0.92
20.83	9.83	10.11	49.67	2.56	0.73	1.604	0.367	0.41	0.57
21.1	10.17	10.14	35.71	2.426	0.79	1.605	0.797	0.36	1.09
21.56	12.30	11.73	182.56	1.91	0.34	1.650	0.773	0.23	2.01
22.29	12.74	12.16	67.60	2.29	0.67	1.622	0.342	0.34	2.65

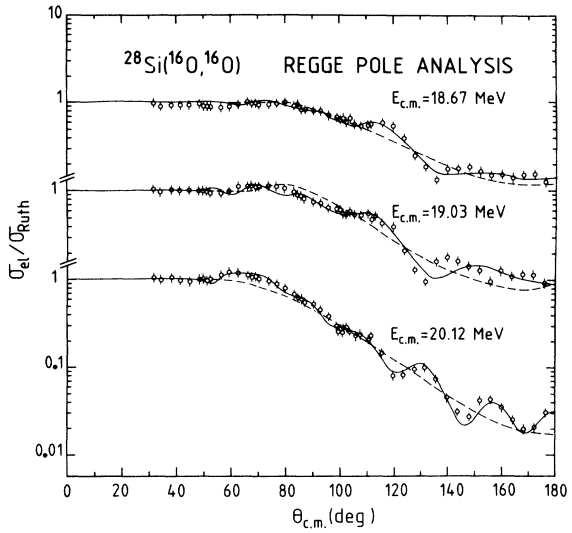

FIG. 9. See the caption of Fig. 7.

difference of behavior is also evident in Figs. 11 and 12 in which the Argand-Cauchy plot for the total S-matrix elements is presented.

Another type of Regge pole analysis has been performed. The diffractional model parameters of Frahn and Venter have been determined at 21.1 MeV, corresponding to the maximum in the excitation function, by fitting only the Fresnel pattern at forward angles. The resulting parameters are $r_0=1.643$ fm, $d=0.600$ fm, and $\mu=2.197$. These parameters called BG-1 have been kept constant for the remaining part of the analysis and only the four parameters of a simple pole have been adjusted in order to best fit the complete angular distributions; the results are presented in Table V. The values of χ^2 are still very acceptable and the fits are indeed very good. It has turned out in this latter analysis that the background angular distributions are lower at backward angles than those of the former analysis. The Regge pole parameters are similar to those of Table IV. The corresponding Argand-Cauchy plots are displayed in Fig. 13. The lines are very smooth since the S-matrix curves are calculated also for noninteger values of the orbital angular momentum l. The

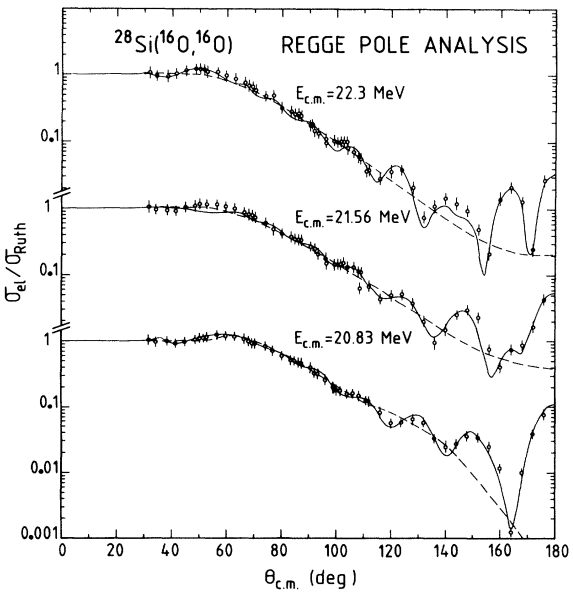

FIG. 10. See the caption of Fig. 7.

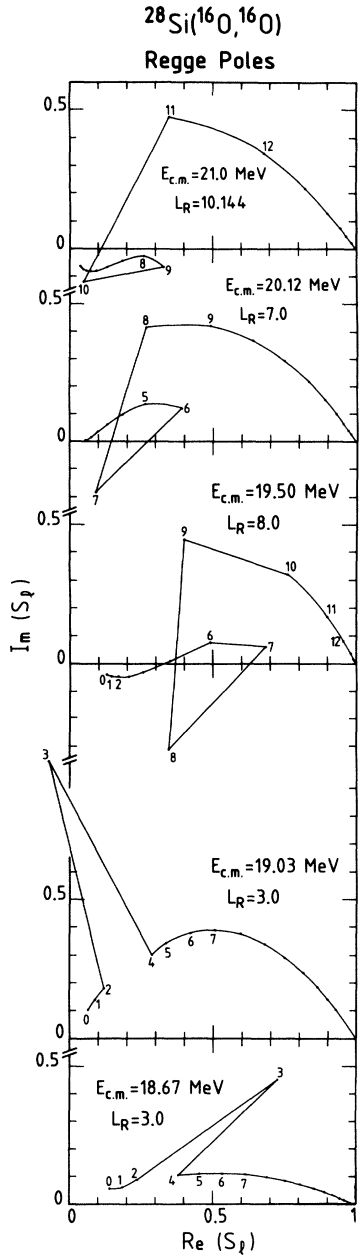

FIG. 11. Argand-Cauchy plot of the total S-matrix elements of the Regge pole analysis of Figs. 7—10—parameters are given in Table III.

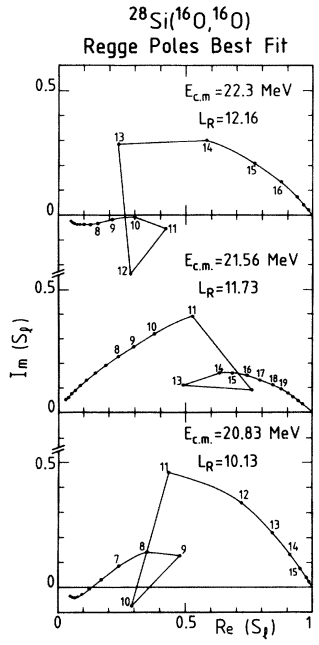

FIG. 12. See the caption of Fig. 11.

loops are very apparent. The physical meaning of Regge pole analysis is that the structure located at 21.1 MeV center of mass energy is described by resonances of several partial waves near the grazing wave. These poles are also qualitatively present in very transparent and deep potentials.[9] Except perhaps at the lowest energies, single partial wave resonances cannot be isolated: they do not provide acceptable fits.

C. Phase shift analysis

For the phase shift analysis, the scattering matrix elements have been written as[3]

$$S_l = S_l(\mathrm{BG}) + \delta S_l \ , \tag{7}$$

with

$$\delta S_l = a_l e^{i\phi_l} \ , \tag{8}$$

where the real numbers a_l and ϕ_l are, respectively, the amplitude and the phase of the deviation of S_l from a standard background at a given energy.

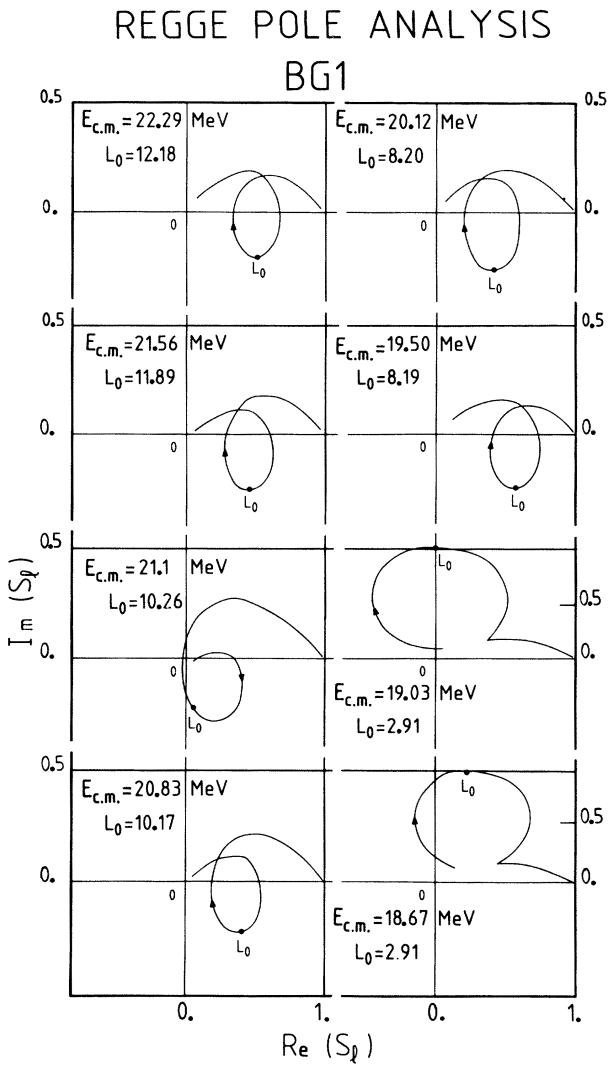

FIG. 13. Argand-Cauchy plot of the total S-matrix element of the Regge pole analysis performed with a common background for all energies. See Table IV for the parameters.

The phase shift analysis of the low energy angular distributions has turned out to be very uncertain since there are several ambiguities. First of all, it is impossible to determine the background from the forward angle Fresnel pattern: different background intensities provide possible

TABLE V. Regge pole analysis parameters.

$E_{c.m.}$ (MeV)	L_g	L_0	ϕ_{l_0}	Γ	D	R_0	d	$\mu/4\Delta$	χ^2
18.67	5.89	2.91	276.4	0.42	0.17	1.643	0.6	0.133	1.56
19.03	6.96	2.91	295.5	0.34	0.16	1.643	0.6	0.150	3.02
19.50	8.15	8.19	108.8	2.57	0.57	1.643	0.6	0.166	5.14
20.12	9.51	8.20	95.9	0.88	0.20	1.643	0.6	0.181	2.45
20.83	10.86	10.17	70.07	2.00	0.50	1.643	0.6	0.194	3.65
21.1	11.17	10.26	53.1	1.97	0.54	1.643	0.6	0.196	4.0
21.56	12.11	11.89	89.1	2.51	0.59	1.643	0.6	0.203	2.82
22.29	13.24	12.18	117.4	1.95	0.43	1.643	0.6	0.209	3.06

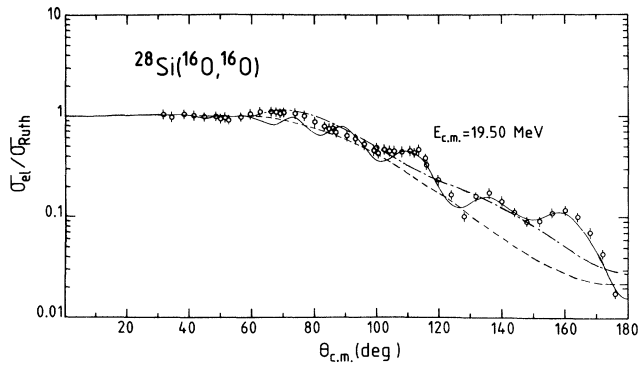

FIG. 14. Phase shift analysis fit (solid curve); the dashed curves are for a common background BG-1 and the dotted-dashed curves for a background adjusted at each energy on the whole angular distribution. (See the text.)

backward angular distributions. Consequently, there is a strong uncertainty in the determination of resonance term magnitudes. Linked to this first problem, two different contiguous terms S_l or S_{l+1} with opposite phase produce very similar fits. Furthermore, an angular distribution involves at least two resonant partial wave terms making the ambiguities extremely large.

The procedure we have used was to try to find the best fits with the minimum numbers of resonant terms $a_l e^{i\phi_l}$ for a given background amplitude. This procedure is obviously quite arbitrary. As previously used for the Regge pole analysis, two different kinds of backgrounds were used: The first one, BG-1, was fixed by fitting the forward angle Fresnel pattern at 21.1 MeV center of mass energy, the second one was fixed by fitting at each energy the whole angular distribution with the diffractional model alone. Figures 14—17 present the best fits to the data obtained with these backgrounds by adding two or three resonant terms; the final results, the solid curves, are the same for both background amplitudes. Of course, the resonant amplitudes and phases which produce the fits are different. The corresponding modulus of total S matrix for the two different kinds of background are plotted in Figs. 18 and 19. We can see on these last two figures that

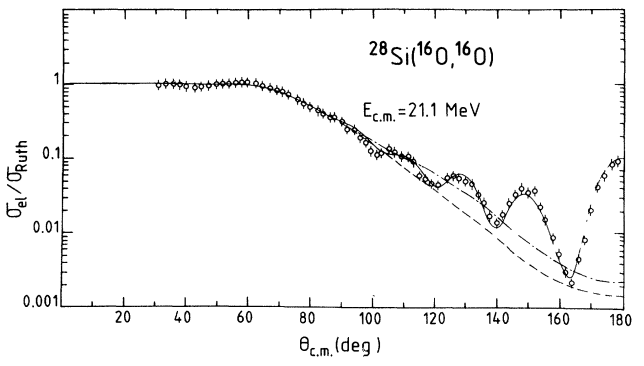

FIG. 15. See the caption of Fig. 14.

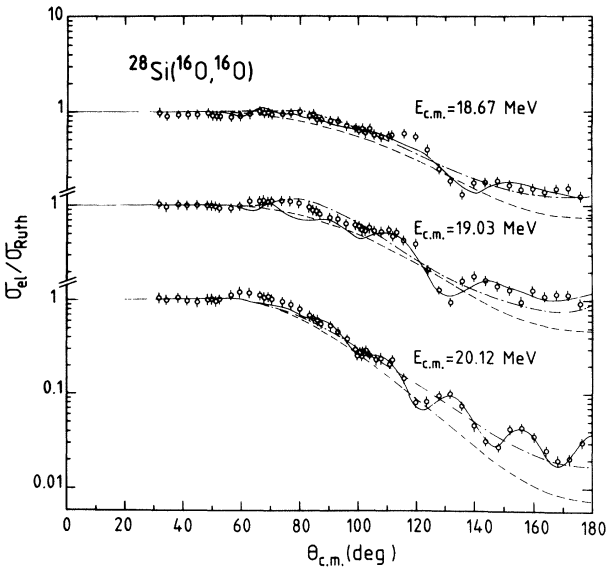

FIG. 16. See the caption of Fig. 14.

at low energy, a $l=3$ resonance is present as in the Regge-pole analysis. At higher energy, around 21 MeV, on the top of the first maxima of the excitation function very good fits are obtained with resonance terms such as $l=6$, 8, and 11, but, unfortunately, $l=6$, 8, and 10 will also produce good fits. As noted previously, assuming resonance terms in other partial waves produces less good but still acceptable fits. Evidently, better fits can be obtained by adding still additional resonant terms. On the other hand, fits with only one resonant term are very poor: two resonant terms are always needed. These various points are illustrated in Table VI at a center of mass ener-

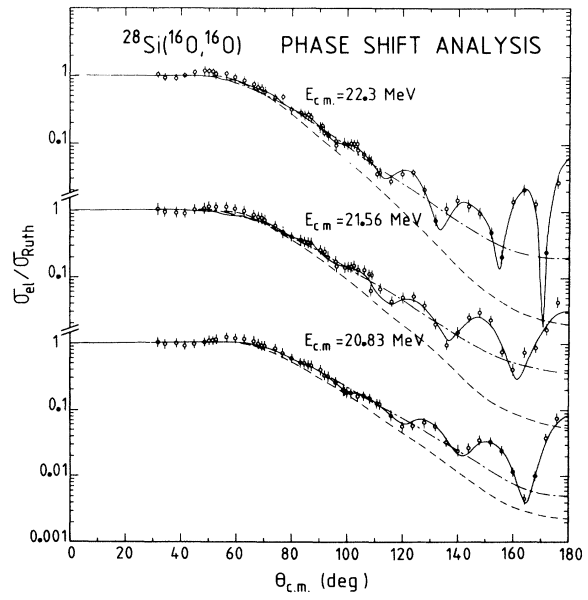

FIG. 17. See the caption of Fig. 14.

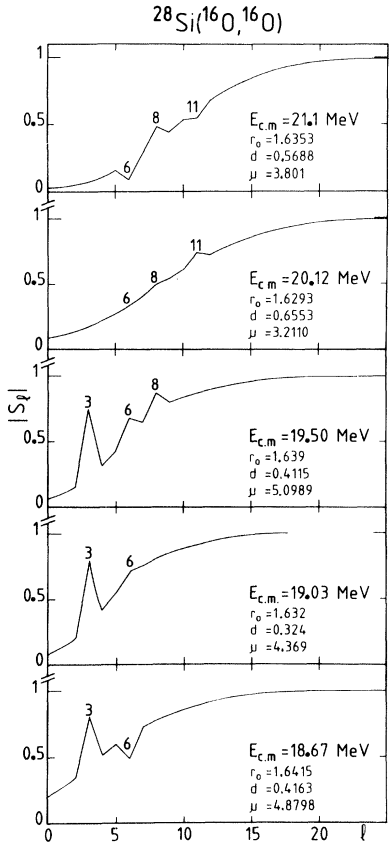

FIG. 18. Modulus of the total scattering element of the phase shift analysis of Figs. 14—17.

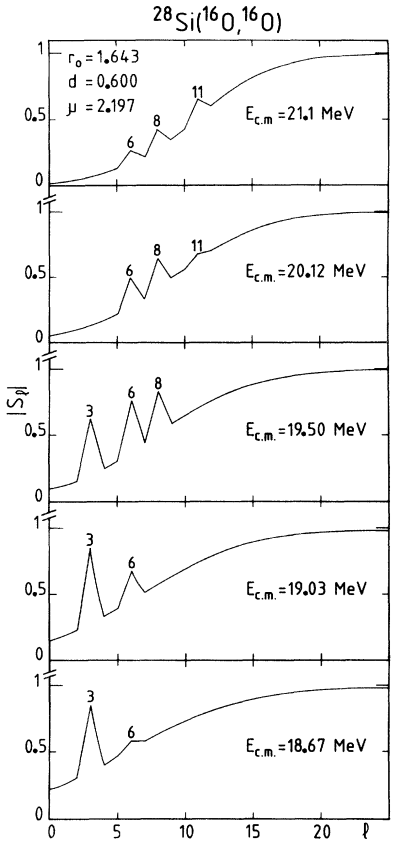

FIG. 19. See the caption of Fig. 18.

TABLE VI. Phase shift analysis parameters. $E_{c.m.}=21.1$ MeV BG^{-1}.

l	a_l	ϕ_l (rad)	χ^2
8	0.21	−0.56	9.46
11	0.16	1.58	11.80
8	0.25	0.04	2.80
11	0.15	1.98	
6	0.17	−0.70	4.33
8	0.13	0.33	
8	0.30	0.46	4.45
10	0.17	0.68	
6	0.12	−0.18	
8	0.16	0.84	1.06
11	0.16	1.10	
8	0.32	1.61	
10	0.27	1.75	2.11
11	0.26	0.67	
6	0.15	0.22	
8	0.24	0.73	2.71
10	0.09	0.04	

gy of 21.1 MeV for the background BG-1. Several fits of the angular distribution are provided for different combinations of resonant terms δS_l; the quality of the fit can be judged by the χ^2 value.

IV. SUMMARY

The three phenomenological analyses presented herein are complementary and self-consistent. The experimental angular distributions can be qualitatively reproduced by an optical model calculation having deep and transparent potentials which exhibit poles. The one Regge pole analysis succeeds also in reproducing the elastic scattering data showing that, in the first structure observed above the Coulomb barrier in the excitation function, several l values contribute to the oscillatory shape of the angular distributions. Phase shift analysis corroborates this last statement and shows that ambiguities in the position of the background scattering allows only tentative spin assignments for the resonant structure.

In conclusion, it appears that a dinuclear system is formed during the collision with a short lifetime and with no definite angular momentum. This dinuclear system exhibits overlapping resonances with spins that may be slightly lower than the grazing partial waves.

[1]P. Braun-Munzinger and J. Barrette, Phys. Rep. 87, 209 (1982); P. Braun-Munzinger, G. M. Berkowitz, M. Gai, J. W. Harris, C. M. Jachcinski, T. R. Renner, and C. O. Uhlhorn, Phys. Rev. C 24, 1010 (1981); J. Barrette, M. J. LeVine, P. Braun-Munzinger, G. M. Berkowitz, M. Gai, J. W. Harris, and J. M. Jachcinski, Phys. Rev. Lett. 40, 445 (1978); C. K. Gelbke, Y. Awess, U. E. P. Berg, J. Barrette, M. J. LeVine, and P. Braun-Munzinger, *ibid.* 41, 1778 (1979); J. Barrette, M. J. LeVine, P. Braun-Munzinger, G. M. Berkowitz, M. Gai, S. W. Harris, C. M. Jachcinski, and C. D. Uhlhorn, Phys. Rev. C 20, 1759 (1979).

[2]A. M. Kobos, G. R. Satchler, and R. S. Mackintosh, Nucl. Phys. A395, 248 (1983).

[3]M. C. Mermaz, Phys. Rev. C 23, 755 (1981).

[4]M. C. Mermaz, A. Greiner, B. T. Kim, M. J. LeVine, E. Müller, M. Ruscev, M. Petrascu, M. Petrovici, and V. Simion, Phys. Rev. C 24, 1512 (1981).

[5]L. C. Northcliffe and R. F. Schilling, Nucl. Data Tables A7, 233 (1970).

[6]J. B. Marion and F. C. Young, *Nuclear Reaction Analysis Graphs and Tables* (North-Holland, Amsterdam, 1968).

[7]S. Kahana, J. Barrette, B. Berthier, E. Chavez, A. Greiner, and M. C. Mermaz, Phys. Rev. C 28, 1393 (1983).

[8]M. J. Jordan, J. V. Maher, and J. C. Peng, Phys. Lett. 87B, 38 (1979); J. C. Peng (private communication).

[9]T. Takemasa and T. Tamura, Phys. Rev. C 18, 1282 (1978); T. Tamura and H. H. Walter, *ibid.* 6, 1976 (1972); C. S. Shastry and I. Parija, *ibid.* 27, 2042 (1983).

[10]N. E. Frahn and R. H. Venter, Ann. Phys. (N.Y.) 24, 243 (1963).